Letter

Nonlinear spectroscopy of bound states in perturbed Ising spin chains

GiBaik Sim,[1,2] Johannes Knolle,[1,2,3] and Frank Pollmann[1,2]

[1]*Department of Physics TQM, Technische Universität München, James-Franck-Straße 1, D-85748 Garching, Germany*

[2]*Munich Center for Quantum Science and Technology (MCQST), 80799 Munich, Germany*

[3]*Blackett Laboratory, Imperial College London, London SW7 2AZ, United Kingdom*

(Received 14 September 2022; revised 20 January 2023; accepted 1 February 2023; published 7 March 2023)

We study the nonlinear response of nonintegrable one-dimensional (1D) spin models using infinite matrix-product state techniques. As a benchmark and demonstration of the method, we first calculate the two-dimensional (2D) coherent spectroscopy for the exactly soluble ferromagnetic transverse field Ising model where excitations are freely moving domain walls. We then investigate the distinct signatures of confined bound states by introducing a longitudinal field and observe the emergence of strong nonrephasinglike signals. To interpret the observed phenomena, we use a two-kink approximation to perturbatively compute the 2D spectra. We find good agreement in comparison with the exact results of the infinite matrix-product state method in the strongly confined regime. We discuss the relevance of our results for quasi-1D Ising spin chain materials, such as $CoNb_2O_6$.

DOI: 10.1103/PhysRevB.107.L100404

Introduction. Spectroscopic tools have played a crucial role in our understanding of complex quantum systems [1]. However, we can only partially measure their correlations with existing tools. One promising direction is to detect the nonlinear response of the target systems which has been utilized to identify the ground-state symmetry of magnetic [2] and superconducting [3,4] materials, geometric phase in topological materials [5–7], novel ground states in correlated systems [8,9], and quasiparticle decay processes in disordered systems [10]. Along this line, *two-dimensional (2D) coherent spectroscopy*, one of the developing spectroscopic tools [11–13], stands out as a technique for a deeper understanding of strongly correlated condensed-matter systems. Besides, recent experimental advances with terahertz sources put the technique in a proper energy range to study rotational dynamics in molecules [14], spin waves in conventional magnets [15], and exotic excitations in quantum magnets [16–20].

In contrast to more common one-dimensional (1D) spectroscopy, the 2D extension unravels not only the optical excitations, but also their interplay [12,13]. The advantage of this experimental technique has been widely adopted by chemists to reveal the structure of complex molecules with great success. However, such achievements rely on powerful numerical methods that help to interpret complicated experimental data starting from concrete microscopic models [21–23]. In this regard, it is desirable to develop an efficient numerical platform for future 2D spectroscopy experiments on quantum magnets similar to the successful use of matrix product state (MPS) techniques for conventional 1D spectroscopy [24–30]. However, the calculation of nonlinear response is less explored and the need for multiple time evolutions makes it much more challenging.

In this Letter, we propose an efficient numerical tool using infinite MPS (iMPS) and study the nonlinear response of the 1D spin model. To benchmark the method, we first focus on the 1D transverse field Ising model (TFIM) whose nonlinear response can be analytically calculated using Jordan-Wigner (JW) transformations [16]. Motivated by the quasi-1D structure of $CoNb_2O_6$—ne of the best material example of an Ising chain magnet—(albeit with more complicated magnetic interactions [29,30]) we then include longitudinal field terms which capture the effects of interchain interactions and lead to the emergence of confined bound-state excitations [31–33]. As a consequence, new signals appear in 2D spectroscopy which include strong nonrephasing and rephasinglike peaks. Our results from the iMPS method are, furthermore, corroborated by perturbative calculations starting from the projected two-kink (TK) low-energy subspace. We find quantitative agreement in the strongly confined regime, which allows us to understand the origin of sharp peaks in the 2D spectrum as transitions between bound states.

Model. We first introduce the 1D TFIM,

$$H_0 = -J \sum_n \sigma_n^z \sigma_{n+1}^z - h^x \sum_n \sigma_n^x, \tag{1}$$

with $J, h_x > 0$. For $h_x < h_x^c = J$, it stabilizes a doubly degenerate ferromagnetic ground state polarized along the easy axis $\hat{z}$. When $h_x > h_x^c$, the system has a unique paramagnetic ground state. In the ferromagnetic regime, the experimental excitation, i.e., a local spin flip, splits into two freely moving kinks (domain walls) between two degenerate states. In the context of nonlinear spectroscopy these fractionalized excitations have been shown to be manifest as sharp signatures in the third-order magnetic susceptibilities [16].

We now include a longitudinal field and focus on the Hamiltonian given by $H = H_0 - h^z \sum_n \sigma_n^z$ with $J, h_x, h_z > 0$. In the ferromagnetic regime, the longitudinal field lifts the degeneracy and selects one of the polarized ground states.

Besides, it induces a linear confining potential between the kinks leading to bound states. As a result, the broad continuum of free kink excitations as probed in linear-response fragments into sharp peaks [34]. At a low transverse field, the splitting can be understood via a Schrödinger equation for the relative kink separation with a linear potential [35] which can also be generalized to include lattice effects [36–42]. The main questions of our Letter are as follows: How to efficiently simulate the nonlinear response of the TFIM with a longitudinal field using MPS methods? What are the robust signatures of confined bound states in nonlinear 2D spectroscopy?

Two-dimensional spectroscopy. Here, we introduce a two-pulse protocol following previous work Ref. [16]. In this setup, two time-domain Dirac-δ pulses B_0 and B_τ which are polarized along $\hat{\alpha}$ and $\hat{\beta}$ directions, respectively, reach the sample at time $T = 0$ and $T = \tau > 0$ successively. These magnetic pulses couple to the local moments of the sample and the induced magnetization along $\hat{\gamma}$ direction is recorded as $M^\gamma_{0\tau}(T)$ at time $T = \tau + t$ where $t > 0$ is the time interval between the second pulse B_τ and the measurement. To subtract the signal from the linear response, two different experiments are repeated but with pulse B_0 or B_τ alone to measure $M^\gamma_0(T)$ and $M^\gamma_\tau(T)$. The nonlinear signal field emerging from the sample at $T = \tau + t$ in the $\hat{\gamma}$ direction is defined as

$$M^\gamma_{NL}(T) \equiv M^\gamma_{0\tau}(T) - M^\gamma_0(T) - M^\gamma_\tau(T). \tag{2}$$

The nonlinear signal depends only on the nonlinear responses and directly measures the second- and higher-order magnetic susceptibilities [19],

$$\begin{aligned} M^\gamma_{\mathrm{NL}}(t,\tau) = {} & \mathcal{B}_0\mathcal{B}_\tau \chi^{(2)}_{\gamma\beta\alpha}(t,\tau+t) \\ & + (\mathcal{B}_0)^2\mathcal{B}_\tau \chi^{(3)}_{\gamma\beta\alpha\alpha}(t,\tau+t,\tau+t) \\ & + \mathcal{B}_0(\mathcal{B}_\tau)^2 \chi^{(3)}_{\gamma\beta\beta\alpha}(t,t,\tau+t) + O(B^4), \end{aligned} \tag{3}$$

where $\mathcal{B}_{0,\tau}$ are the spatial areas of the pulse $B_{0,\tau}$.

The 2D spectrum is the Fourier transform of $M^\gamma_{\mathrm{NL}}(t,\tau)$ over both time domains t and τ. In Eq. (3), the leading contribution to the nonlinear response in the two-pulse setup, i.e., the second-order nonlinear susceptibility $\chi^{(2)}_{\gamma\beta\alpha}(t,\tau+t)$ is given as

$$\begin{aligned} \chi^{(2)}_{\gamma\beta\alpha}(t,\tau+t) = -\frac{\theta(t)\theta(\tau)}{4L}\mathrm{Re}\sum_{j,l,m}\big[& S^{\gamma\beta\alpha}_{j,l,m}(\tau+t,\tau,0) \\ & - S^{\beta\gamma\alpha}_{j,l,m}(\tau,\tau+t,0)\big], \end{aligned} \tag{4}$$

with the three-point spin-correlation function in the ground-state $|\psi\rangle$,

$$S^{\gamma\beta\alpha}_{j,l,m}(T_1,T_2,0) = \langle\psi|\sigma^\gamma_j(T_1)\sigma^\beta_l(T_2)\sigma^\alpha_m(0)|\psi\rangle, \tag{5}$$

where $\sigma^\gamma_j(T) \equiv e^{iHT}\sigma^\gamma_j e^{-iHT}$. When the Hamiltonian and $|\psi\rangle$ preserve the lattice translation symmetry, the site index m in Eqs. (4) and (5) can be fixed, e.g. as $c \equiv L/2$ the central site of the system, which we use in the following. Then, $\chi^{(2)}_{\gamma\beta\alpha}(t,\tau+t)$ is obtained by evaluating:

$$-\frac{\theta(t)\theta(\tau)}{4}\mathrm{Re}\sum_{j,l}\big[S^{\gamma\beta\alpha}_{j,l,c}(\tau+t,\tau,0) - S^{\beta\gamma\alpha}_{j,l,c}(\tau,\tau+t,0)\big]. \tag{6}$$

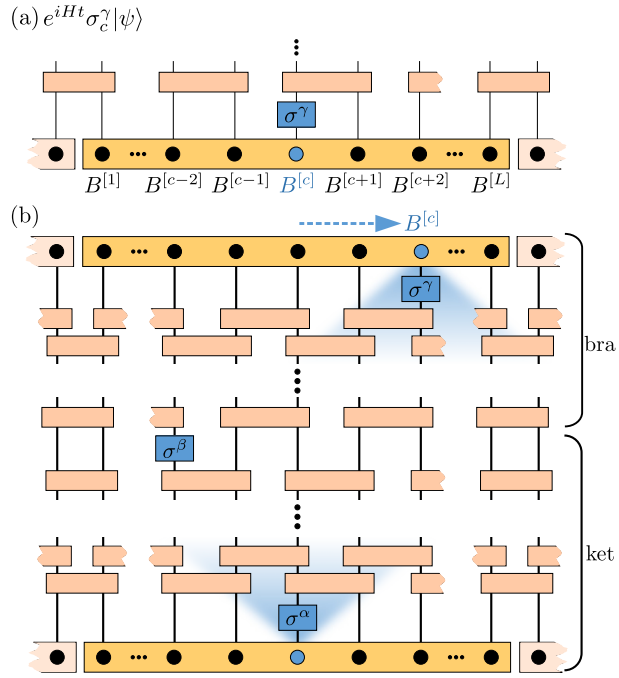

FIG. 1. Exploiting infinite boundary conditions for translation-invariant systems, two real-time evolution runs are sufficient to evaluate $\sum_{j,l} S^{\gamma\beta\alpha}_{j,l,c}(\tau+t,\tau,0)$. (a) iMPS representation of a state $e^{iHt}\sigma^\gamma_c|\psi\rangle$ with L sites in the unit cell. (b) Transfer matrix of two distinct iMPS "bra" and "ket" which represent $e^{iHt}\sigma^\gamma_{c+2}|\psi\rangle$ and $\sigma^\beta_{c-2}e^{-iH\tau}\sigma^\alpha_c|\psi\rangle$ respectively. The color gradient illustrates the light cone spreading of correlations following a local quench.

Method. A promising tool for calculating $S^{\gamma\beta\alpha}_{j,l,c}(\tau+t,\tau,0)$ in Eq. (6) for a whole range of site indices j and l is to use the iMPS method. We only need to perform two different real-time evolution runs to calculate $\sum_{j,l} S^{\gamma\beta\alpha}_{j,l,c}(\tau+t,\tau,0) = \sum_{j,l} e^{iE(\tau+t)}\langle\psi|\sigma^\gamma_j e^{-iHt}\sigma^\beta_l e^{-iH\tau}\sigma^\alpha_c|\psi\rangle$ where E is the ground-state energy. In addition, finite-size effects are avoided. Such effect originates from the bouncing of correlations following a local quench at site $j = 1$ or L, boundary sites of the system. Below, we explain a procedure to obtain $\langle\psi|\sigma^\gamma_j e^{-iHt}\sigma^\beta_l e^{-iH\tau}\sigma^\alpha_c|\psi\rangle$ [see Appendix A for $S^{\beta\gamma\alpha}_{j,l,c}(\tau,\tau+t,0)$].

(1) Find a ground state and perform a time evolution following a local quench, σ^γ_c or σ^α_c, using the infinite-time evolving block decimation (iTEBD) method [43–45] to obtain an iMPS for $e^{iHt}\sigma^\gamma_c|\psi\rangle$, which is shown in Fig. 1(a), or $e^{-iH\tau}\sigma^\alpha_c|\psi\rangle$.

(2) Shift every B tensor of an iMPS, which represents $e^{iHt}\sigma^\gamma_c|\psi\rangle$, $(c-j)$ sites to the right within a window of size L to obtain a new iMPS bra associated with $e^{iHt}\sigma^\gamma_j|\psi\rangle$.

(3) Apply a local operator σ^β_l to an iMPS associated with $e^{-iH\tau}\sigma^\alpha_c|\psi\rangle$ and get a new iMPS ke which represents $\sigma^\beta_l e^{-iH\tau}\sigma^\alpha_c|\psi\rangle$.

(4) Evaluate an overlap of two iMPS bra and ket within the window by calculating the dominant left and right eigenvectors of the corresponding transfer matrix, which is shown in Fig. 1(b), and obtain $\langle\psi|\sigma^\gamma_j e^{-iHt}\sigma^\beta_l e^{-iH\tau}\sigma^\alpha_c|\psi\rangle$ [34].

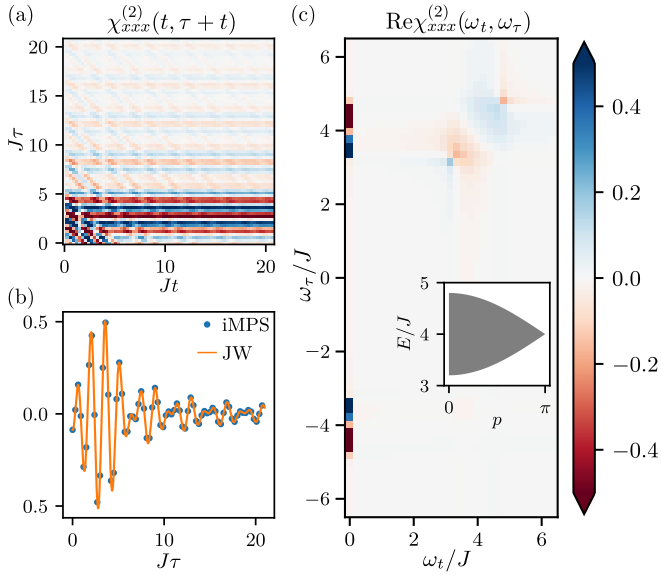

FIG. 2. Second-order susceptibility in the ferromagnetic phase of the TFIM with $h_x/J = 0.2$. (a) $\chi^{(2)}_{xxx}(t, \tau + t)$ from iMPS method with a window of size $L = 80$. The data are rescaled such that the maximal absolute value is 1. (b) $\chi^{(2)}_{xxx}(t, \tau + t)$ at $Jt = 15$ from iMPS method and JW formalism. For the latter case, we set a size of the system $L = 80$ with PBC. (c) Real part of Fourier-transformed $\chi^{(2)}_{xxx}(t, \tau + t)$. The inset: TK excitation continua of the TFIM.

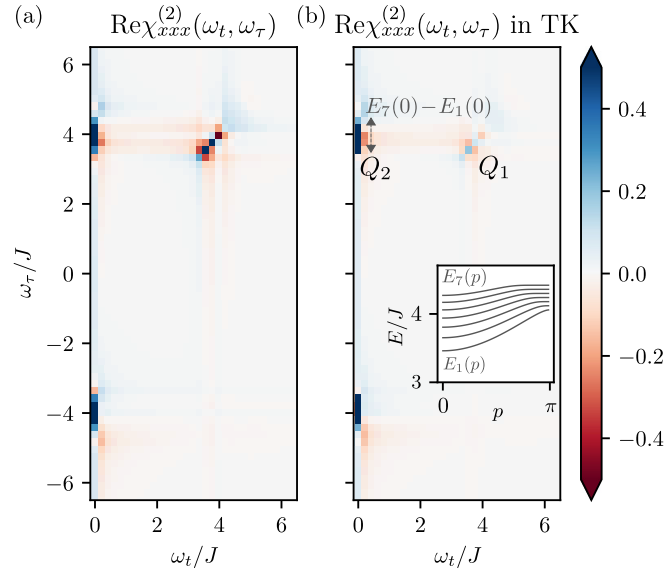

FIG. 3. The 2D spectra $\chi^{(2)}_{xxx}(\omega_t, \omega_\tau)$ of TFIM with the longitudinal field for $h_x/J = 0.2$ and $h_z/J = 0.03$. For the spectra, the first and fourth quadrants are only shown. The other half are obtained by complex conjugation. (a) Result of the iMPS method. (b) Result of perturbative calculation within the projected TK subspace. The inset: The dispersion relation $E_n(p)$ in momentum space of the seven lowest bands of TK bound states in the weakly confined regime. $E_n(p)$ is given in Eq. (13).

Before investigating the 2D spectrum of the nonintegrable TFIM with the longitudinal field, we first focus on the free TFIM and compare the result of $\chi^{(2)}_{xxx}(t, \tau + t)$ using two different schemes, i.e., the numerical iMPS method and analytic calculations via the JW transformation with the periodic boundary condition (PBC). Here and below, we set $h_x/J = 0.2$ and all iMPS simulations are performed with a spatial window of size $L = 80$ sites and over the time-range $Jt, J\tau = 30$. Within such temporal range, the light cone spreading of correlations, which follows a local quench at the center of a spatial window, does not reach the boundary of the window. In Fig. 2(a), we plot the result of $\chi^{(2)}_{xxx}(t, \tau + t)$ from the iMPS method. In order to check the errors of our method, we tracked the truncation error, the truncated weight of many-body wave function at each time step in iTEBD, which quantifies an upper limit for the truncation effect on local observables ($\lesssim 10^{-8}$ for every result given in our Letter). Besides, we also followed the dependence of $\chi^{(2)}_{xxx}(t, \tau + t)$ on the time-step δt and the bond dimension χ, fixing to $\delta t = 0.03/J$ and $\chi_{\max} = 30$. In Fig. 2(b), we compare $\chi^{(2)}_{xxx}(t, \tau + t)$ at $Jt = 15$ from the iMPS method with the one from the JW formalism which confirms exact agreement. In Fig. 2(c), we plot Re $\chi^{(2)}_{xxx}(\omega_t, \omega_\tau)$, the real part of the Fourier-transformed $\chi^{(2)}_{xxx}(t, \tau + t)$. It contains a sharp vertical line of intensity centered at $\omega_t = 0$. Regarding ω_t and ω_τ as the detecting and pumping frequencies, the response is known as a rectification signal.[1] It also contains a diffusive, weak nonrephasing signal[2] in the first frequency quadrant, mirroring the energy range of the free TK continuum, which is shown in the inset of Fig. 2(c) [16].

Results. Next, we focus on the 2D spectrum of the 1D TFIM with the longitudinal field using the iMPS method. Figure 3(a) shows the Re $\chi^{(2)}_{xxx}(\omega_t, \omega_\tau)$, which is calculated in weakly confined regime with $h_z/J = 0.03$ (see Appendix B for the Im $\chi^{(2)}_{xxx}(\omega_t, \omega_\tau)$, which is related to the Re $\chi^{(2)}_{xxx}(\omega_t, \omega_\tau)$ by the dispersion relation [46–48]). This value is similar to the one used in Ref. [36] to describe $CoNb_2O_6$. New spectroscopic signals are encoded in $\chi^{(2)}_{xxx}(\omega_t, \omega_\tau)$ in the presence of a longitudinal field. First, it contains a dominant nonrephasing signal which appears as diagonal peaks in the first quadrant. At the same time, a weakly diffusive terahertz rectification signal is also detected as a streak along the ω_τ axis. In Fig. 4(a), we plot Re $\chi^{(2)}_{xxx}(\omega_t, \omega_\tau)$ in a strongly confined regime with $h_z/J = 0.4$. Unlike the previous regime, it contains a nonrephasing, such as the signal which appears as strong cross (off-diagonal) peaks in the first quadrant. Besides, a subdominant rephasing like signal appears as cross peaks in the fourth quadrant.

Few-kink effective description and interpretation. To interpret the 2D spectra, we use a projected TK model and can study the excitations of Eq. (1) perturbatively [38,41]. The idea is to project the full Hilbert space down to the Hilbert space of TK states where regions of opposite

[1]The term rectification signal is used to denote signals which oscillate in time as $e^{-iE\tau}$ for some E's [15,16].

[2]The term rephasing (nonrephasing) signal is commonly used in nonlinear optics to denote signals which oscillate in time as $e^{-iE(t-\tau)}$ ($e^{-iE(t+\tau)}$) [12,13].

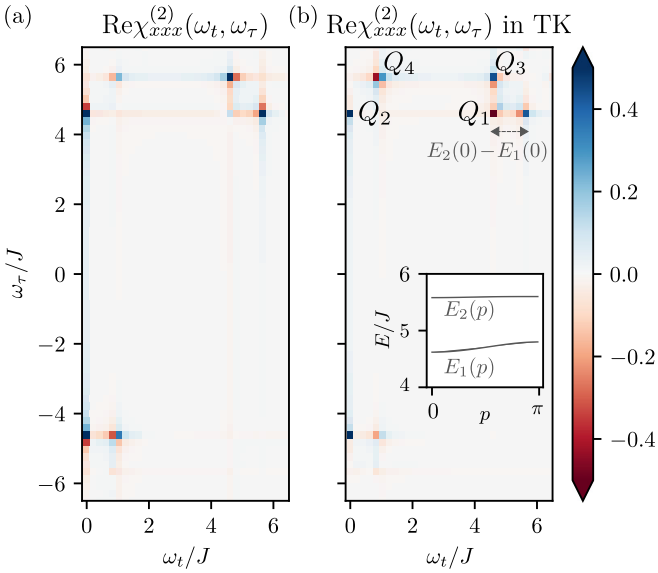

FIG. 4. The 2D spectra $\chi^{(2)}_{xxx}(\omega_t,\omega_\tau)$ of TFIM with the longitudinal field for $h_x/J=0.2$ and $h_z/J=0.4$ (a) Result of iMPS method. (b) Result of perturbative method. The inset: The dispersion relation $E_n(p)$ in momentum space of the two lowest bands of TK bound states in the strongly confined regime. $E_n(p)$ is given in Eq. (13).

magnetization are separated by the two different domain walls. In this model, each TK state is represented as $|j,l\rangle \equiv |\cdots\uparrow\uparrow\downarrow_j\downarrow\cdots\downarrow\downarrow_{(j+l-1)}\uparrow\uparrow\cdots\rangle$, where j is the starting site of down spins. The TK model has been adopted to phenomenologically understand the confinement of excitations observed in the dynamical (1D) neutron response of $CoNb_2O_6$ [36,38]. The projected model is expected to capture the low-energy excitations of the original model quantitatively well as long as $h_x/J \ll h_z/J$. This can be understood by looking into the energy gap between TK states and four-kink states [49]. We adopt the model also in a weakly confined regime $h_x/J \geqslant h_z/J$ to investigate the qualitative structure of 2D spectra and to help the understanding of the exact iMPS result. The TK Hamiltonian $\mathcal{H}_{TK} \equiv \mathcal{P}H\mathcal{P}$ with projector $\mathcal{P}$ acts as follows:

$$\mathcal{H}_{TK}|j,l\rangle = 4J|j,l\rangle - h_x[|j,l+1\rangle + |j,l-1\rangle + |j+1,l-1\rangle + |j-1,l+1\rangle] + 2h_z l|j,l\rangle. \tag{7}$$

For our translational invariant model, the total momentum p of the bound state is a good quantum number. In the momentum basis $|p,l\rangle = \sum_j \exp(ipj)|j,l\rangle$, the Hamiltonian is diagonal in p and acts on $|p,l\rangle$ as

$$\mathcal{H}_{TK}|p,l\rangle = 4J|p,l\rangle - h_x[(1+e^{ip})|p,l+1\rangle + (1+e^{-ip})|p,l-1\rangle] + 2h_z l|p,l\rangle. \tag{8}$$

The eigenequation with the excitation energy $E_n(p)$ takes the form as

$$\mathcal{H}_{TK}|\Phi_n(p)\rangle = E_n(p)|\Phi_n(p)\rangle, \tag{9}$$

where

$$|\Phi_n(p)\rangle \equiv \sum_{l=1}^{\infty} \exp\left(\frac{ipl}{2}\right)\psi_n(l,p)|p,l\rangle \Big/ \sqrt{\sum_{l=1}^{\infty}|\psi_n(l,p)|^2}$$

with discrete band index n. Equation (9) can be expanded as

$$[4J + 2h_z l - E_n(p)]\psi_n(l,p) - 2h_x\cos(p/2) \times[\psi_n(l+1,p)+\psi_n(l-1,p)] = 0. \tag{10}$$

Equation (10) can be rewritten as

$$(-\lambda_n + \mu l)\psi_n(l,p) - \frac{\psi_n(l+1,p)+\psi_n(l-1,p)}{2} = 0, \tag{11}$$

where

$$\lambda_n \equiv \frac{E_n(p)-4J}{4h_x\cos(p/2)}, \qquad \mu \equiv \frac{h_z}{2h_x\cos(p/2)},$$

with the boundary conditions, $\lim_{l\to 0}\psi_n(l,p)=0$ and $\lim_{l\to+\infty}\psi_n(l,p)=0$. The solution of Eq. (11) reads as

$$\lambda_n = -\mu\nu_n. \tag{12}$$

Here, ν_n is the solution of the equation $J_{\nu_n}(1/\mu)=0$ where $J_\nu(x)$ is the Bessel function of order ν [38]. Then, the excitation energy $E_n(p)$ reads as

$$E_n(p) = 4J - 2h_z\nu_n. \tag{13}$$

Now, $\sum_{j,k,l} S^{xxx}_{j,k,l}(\tau+t,\tau,0)$ can be calculated within the TK subspace as

$$\begin{aligned}
&\sum_{j,k,l} S^{xxx}_{j,k,l}(\tau+t,\tau,0) \\
&= \sum_{j,k,l}\langle\psi|e^{iH(\tau+t)}\sigma^x_j e^{-iHt}\sigma^x_k e^{-iH\tau}\sigma^x_l|\psi\rangle \\
&= \sum_{j,k,l}\sum_{n,m,p,q} e^{-i(E_n(p)t+E_m(q)\tau)}\langle\psi|\sigma^x_j|\Phi_n(p)\rangle \\
&\quad\times\langle\Phi_n(p)|\sigma^x_k|\Phi_m(q)\rangle\langle\Phi_m(q)|\sigma^x_l|\psi\rangle \\
&= \sum_{j,k,l}\sum_{n,m,p} e^{-i(E_n(p)t+E_m(p)\tau)}\langle\psi|\sigma^x_j|\Phi_n(p)\rangle \\
&\quad\times\langle\Phi_n(p)|\sigma^x_k|\Phi_m(p)\rangle\langle\Phi_m(p)|\sigma^x_l|\psi\rangle
\end{aligned} \tag{14}$$

where $|\psi\rangle$ is the nondegenerate ferromagnetic ground state with no kinks. Here, $\sum_k\langle\Phi_n(p)|\sigma^x_k|\Phi_m(p)\rangle$ can be expanded as

$$\frac{\sum_{k,l',l}\langle p,l'|\sigma^x_k|p,l\rangle e^{-ip(l'-l)/2}\psi_n(l',p)\psi_m(l,p)}{\sqrt{\sum_{l=1}^{\infty}|\psi_n(l,p)|^2}\sqrt{\sum_{l=1}^{\infty}|\psi_m(l,p)|^2}}, \tag{15}$$

with

$$\langle p,l'|\sigma^x_k|p,l\rangle = \sum_{j',j}\exp[-ip(j'-j)]\langle j',l'|\sigma^x_k|j,l\rangle. \tag{16}$$

Equation (16) clearly shows that $\langle\Phi_n(p)|\sigma^x_k|\Phi_m(p)\rangle$ is finite only when one of the following four conditions is met:

1. $|j,l\rangle = |k+1,l\rangle, \quad |j',l'\rangle = |k,l+1\rangle,$
2. $|j,l\rangle = |k-l,l\rangle, \quad |j',l'\rangle = |k-l,l+1\rangle,$
3. $|j,l\rangle = |k,l\rangle, \quad |j',l'\rangle = |k+1,l-1\rangle,$
4. $|j,l\rangle = |k-l+1,l\rangle, \quad |j',l'\rangle = |k-l+1,l-1\rangle.$

Then, $\sum_k \langle \Phi_n(p)|\sigma_k^x|\Phi_m(p)\rangle$ can be simplified as

$$\frac{\sum_l \cos\frac{p}{2}[\psi_n(l,p)\psi_m(l+1,p)+\psi_n(l,p)\psi_m(l-1,p)]}{\sqrt{\sum_{l=1}^{\infty}|\psi_n(l,p)|^2}\sqrt{\sum_{l=1}^{\infty}|\psi_m(l,p)|^2}}. \tag{17}$$

To formulate Eq. (19), we first rewrite Eq. (11) with two different band indices, n and m,

$$(-\lambda_n+\mu l)\psi_n(l,p)=\frac{\psi_n(l+1,p)+\psi_n(l-1,p)}{2}, \tag{18}$$

$$(-\lambda_m+\mu l)\psi_m(l,p)=\frac{\psi_m(l+1,p)+\psi_m(l-1,p)}{2}. \tag{19}$$

Now, we multiply $\psi_m(l+1,p)$ to Eq. (20) and $\psi_n(l-1,p)$ to Eq. (21), subtract one from the other, and sum it over n. Then, we get

$$\sum_l \psi_n(l,p)\psi_m(l+1,p)=\frac{-2}{\lambda_n-\lambda_m-\mu}, \tag{20}$$

where we set $\psi_n(1,p)=-2$ without loss of generality [38]. We can proceed similarly and obtain

$$\sum_l \psi_n(l,p)\psi_m(l-1,p)=\frac{-2}{\lambda_m-\lambda_n-\mu}. \tag{21}$$

In the end, we obtain $\sum_{j,k,l} S^{xxx}_{jkl}(\tau+t,\tau,0)$ within the TK subspace as

$$\sum_{n,m,p} C_{n,m}(p)e^{-i[E_n(p)t+E_m(p)\tau]}, \tag{22}$$

with the optical matrix element,

$$C_{n,m}(p)\equiv -2\cos\frac{p}{2}\left(\frac{1}{\lambda_m-\lambda_n-\mu}+\frac{1}{\lambda_n-\lambda_m-\mu}\right)\times I_n(p)I_m(p). \tag{23}$$

Here, the relative intensity of the nth mode is defined as

$$I_n(p)\equiv\frac{|\psi_n(1,p)|^2}{\sum_{l=1}^{\infty}|\psi_n(l,p)|^2}=\frac{4}{\sum_{l=1}^{\infty}|\psi_n(l,p)|^2}=2\mu\left\{\frac{\partial}{\partial\nu}\left[\frac{J_\nu(1/\mu)}{J_{\nu+1}(1/\mu)}\right]\right\}^{-1}\Bigg|_{\nu\to\nu_n}. \tag{24}$$

Similarly, we can express $\sum_{j,k,l} S^{xxx}_{jkl}(\tau,\tau+t,0)$ within the TK subspace as

$$\sum_{n,m,p} C_{n,m}(p)e^{-iE_m(p)\tau}e^{-i[E_m(p)-E_n(p)]t}. \tag{25}$$

With Eqs. (24) and (25), we obtain

$$\chi^{(2)}_{xxx}(t,\tau+t)=\theta(t)\theta(\tau)(Q_1+Q_2+Q_3+Q_4), \tag{26}$$

with

$$Q_1=\sum_{n,p} C_{n,n}(p)\cos[E_n(p)(t+\tau)],$$

$$Q_2=\sum_{n,p} C_{n,n}(p)\cos[E_n(p)\tau],$$

$$Q_3=\sum_{n\neq m,p} C_{n,m}(p)\cos[E_n(p)t+E_m(p)\tau],$$

$$Q_4=\sum_{n\neq m,p} C_{n,m}(p)\cos\{[E_n(p)-E_m(p)]t-E_m(p)\tau\}.$$

The interpretation of 2D spectra now becomes transparent: Q_1 gives rise to diagonal nonrephasing peaks at $\omega_t,\omega_\tau=E_n(p)$, and Q_2 produces dominant terahertz rectification signals at $\omega_t=0$ and $\omega_\tau=\pm E_m(p)$ [Figs. 3(b) and 4(b)]. In the strongly confined regime, Q_3 gives rise to dominant cross peaks in the first frequency quadrant originating from the nonrephasinglike process [Fig. 4(b)]. To be more precise, such peaks sharply appear at $\omega_t=E_1(0)$ and $\omega_\tau=E_2(0)$ or $\omega_t=E_2(0)$ and $\omega_\tau=E_1(0)$, indicating the presence of different TK excited states. Such sharp peaks do not appear in the free 1D TFIM, which can be mapped to independent two-level systems with each having a single excited state [16]. Q_4 contains terms which induce sharp rephasing- (nonrephasing-) like signals in the fourth (first) frequency quadrants which are visible in the strongly confined regime [Fig. 4(b)]. Such signals also originate from the presence of different TK excited states and appear at $\omega_t=E_2(0)-E_1(0)$, an energy gap between first and second excited states, and $\omega_\tau=E_2(0)$ or $-E_1(0)$, see the inset.

Conclusions. In the present Letter, we have developed an iMPS method for calculating the nonlinear response of 1D spin systems. As a demonstration, we calculated the second-order susceptibility, which dominates the nonlinear response for the ferromagnetic 1D TFIM where a single spin flip is fractionalized into two freely moving domain walls. We benchmarked our numerical results with exact analytical calculations. We then included a longitudinal field, which induces a linear confining potential between kink excitations. In the presence of a longitudinal field, the second-order susceptibility contains new signals which give rise to strong nonrephasing- and rephasinglike peaks. To understand the emergence of such signals, we employ a simplified two-kink description, which describes the low-energy excitations in the strongly confined regime and calculates the second-order susceptibility perturbatively. The approximate method captures the nonlinear response of the system in the strongly confined regime and allows for a simple interpretation.

As a future direction, it would be interesting to apply our iMPS method near the quantum critical point between the ferromagnetic and the paramagnetic states where a hidden E_8 symmetry emerges [34,36]. A crucial question regards then the existence of robust signals in 2D spectrum which detect the emergent symmetry. Regarding the microscopic description and three-dimensional nature of $CoNb_2O_6$ [36,37] ($BaCo_2V_2O_8$ [50,51]); it would be interesting to study a more quantitative model [29,30] and go beyond simple chains, e.g., by extending these to coupled Ising ladders [37]. Terahertz 2D coherent spectroscopy holds the promise of

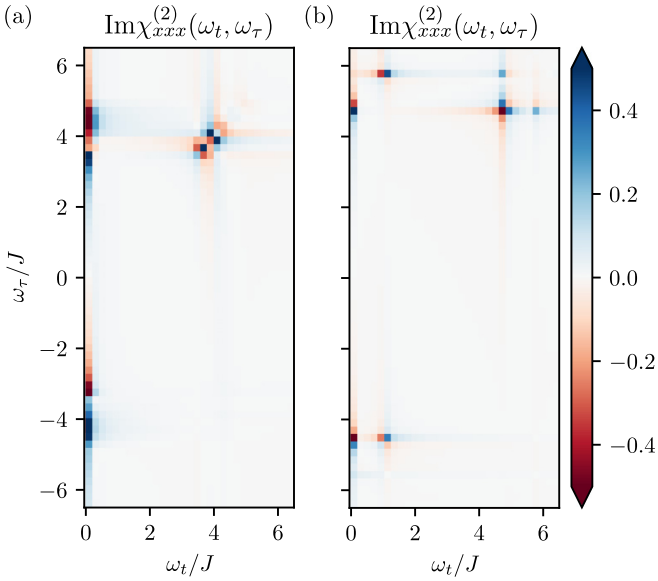

FIG. 5. The 2D spectra $\chi^{(2)}_{xxx}(\omega_t,\omega_\tau)$ of TFIM with $h_x/J=0.2$ and (a) $h_z/J=0.03$ and (b) $h_z/J=0.4$.

uncovering the nature of exotic excitations in strongly correlated quantum materials. A challenging but very worthwhile direction will be an extension of our method to quantum magnets beyond one dimension where the nature of fractionalized excitations and confinement thereof remains poorly understood.

Note added. When finalizing the Letter, related works appeared that investigate nonlinear response from quasiparticle interactions [52,53].

Acknowledgments. We thank N. P. Armitage, R. Coldea, M. Drescher, H.-K. Jin, and W. Choi for insightful discussions related to this Letter. G.B.S. was funded by the European Research Council (ERC) under the European Unions Horizon 2020 Research and Innovation Program (Grant Agreement No. 771537). F.P. acknowledges support of the Deutsche Forschungsgemeinschaft (DFG, German Research Foundation) under Germany's Excellence Strategy Grant No. EXC-2111-390814868. J. K. acknowledges support from the Imperial-TUM flagship partnership. The research is part of the Munich Quantum Valley, which is supported by the Bavarian state government with funds from the Hightech Agenda Bayern Plus. Tensor network calculations were performed using the TeNPy Library [54].

APPENDIX A: A PROCEDURE TO OBTAIN $S^{\beta\gamma\alpha}_{j,l,c}(\tau,\tau+t,0)$ WITH THE IMPS METHOD

In this Appendix, we provide steps to calculate $S^{\beta\gamma\alpha}_{j,l,c}(\tau,\tau+t,0)=e^{iE\tau}\langle\psi|\sigma^\beta_j e^{iHt}\sigma^\gamma_l e^{-iH(\tau+t)}\sigma^\alpha_c|\psi\rangle$ using the iMPS.

(1) Find an iMPS approximation of the ground-state $|\psi\rangle$ with energy E [55,56].

(2) Allow the tensors of the iMPS with a spatial window of size L to vary in time as in Refs. [57–60].

(3) Apply a local operator σ^β_c (σ^α_c) at the center of the window to get $\sigma^\beta_c|\psi\rangle$ ($\sigma^\alpha_c|\psi\rangle$).

(4) Perform a real time evolution following the local quench σ^β_c (σ^α_c) using the iTEBD method [43–45] to obtain an iMPS which represents $e^{-iHt}\sigma^\beta_c|\psi\rangle$ ($e^{-iH(\tau+t)}\sigma^\alpha_c|\psi\rangle$).

(5) Shift every B tensor of an iMPS, which represents $e^{-iHt}\sigma^\beta_c|\psi\rangle$, $(c-j)$ sites to the right within the window to obtain a new iMPS bra associated with $e^{-iHt}\sigma^\beta_j|\psi\rangle$.

(6) Apply an operator σ^γ_l to an iMPS, which approximates $e^{-iH(\tau+t)}\sigma^\alpha_c|\psi\rangle$ and get a new iMPS ket associated with $\sigma^\gamma_l e^{-iH(\tau+t)}\sigma^\alpha_c|\psi\rangle$.

(7) Evaluate an overlap of two iMPS bra and ket within the window by calculating the dominant eigenvalue of the corresponding transfer matrix to obtain $\langle\psi|\sigma^\beta_j e^{iHt}\sigma^\gamma_l e^{-iH(\tau+t)}\sigma^\alpha_c|\psi\rangle$.

(8) Multiply $e^{iE\tau}$ and $\langle\psi|\sigma^\beta_j e^{iHt}\sigma^\gamma_l e^{-iH(\tau+t)}\sigma^\alpha_c|\psi\rangle$.

APPENDIX B: IMAGINARY PART OF $\chi^{(2)}_{xxx}(\omega_t,\omega_\tau)$

In this Appendix, we focus on $\mathrm{Im}\,\chi^{(2)}_{xxx}(\omega_t,\omega_\tau)$ in the ferromagnetic phase of the Ising model. In Fig. 5(a), we plot $\mathrm{Im}\,\chi^{(2)}_{xxx}(\omega_t,\omega_\tau)$ in the weakly confined regime with $h_x/J=0.2$ and $h_z/J=0.03$. We use the iMPS method to obtain the real-time correlation functions $\chi^{(2)}_{xxx}(t,\tau+t)$ and perform fast Fourier transformations. One can clearly observe the emergence of strong nonrephasing signals in the first frequency quadrant. Figure 5(b) shows $\mathrm{Im}\,\chi^{(2)}_{xxx}(\omega_t,\omega_\tau)$ in the strongly confined regime with $h_x/J=0.2$ and $h_z/J=0.4$. Similar to the real part, it contains cross peaks which include rephasinglike and nonrephasinglike signals.

[1] T. P. Devereaux and R. Hackl, Rev. Mod. Phys. **79**, 175 (2007).
[2] M. Fiebig, V. V. Pavlov, and R. V. Pisarev, J. Opt. Soc. Am. B **22**, 96 (2005).
[3] H. Chu, M.-J. Kim, K. Katsumi, S. Kovalev, R. D. Dawson, L. Schwarz, N. Yoshikawa, G. Kim, D. Putzky, Z. Z. Li *et al.*, Nat. Commun. **11**, 1793 (2020).
[4] L. Schwarz, B. Fauseweh, N. Tsuji, N. Cheng, N. Bittner, H. Krull, M. Berciu, G. Uhrig, A. Schnyder, S. Kaiser *et al.*, Nat. Commun. **11**, 287 (2020).
[5] L. Wu, S. Patankar, T. Morimoto, N. L. Nair, E. Thewalt, A. Little, J. G. Analytis, J. E. Moore, and J. Orenstein, Nat. Phys. **13**, 350 (2017).
[6] Y. Shao, R. Jing, S. H. Chae, C. Wang, Z. Sun, E. Emmanouilidou, S. Xu, D. Halbertal, B. Li, A. Rajendran *et al.*, Proc. Natl. Acad. Sci. USA **118**, e2116366118 (2021).
[7] P. He, H. Isobe, D. Zhu, C.-H. Hsu, L. Fu, and H. Yang, Nat. Commun. **12**, 698 (2021).
[8] L. Zhao, C. Belvin, R. Liang, D. Bonn, W. Hardy, N. Armitage, and D. Hsieh, Nat. Phys. **13**, 250 (2017).
[9] L. Zhao, D. Torchinsky, H. Chu, V. Ivanov, R. Lifshitz, R. Flint, T. Qi, G. Cao, and D. Hsieh, Nat. Phys. **12**, 32 (2016).
[10] F. Mahmood, D. Chaudhuri, S. Gopalakrishnan, R. Nandkishore, and N. Armitage, Nat. Phys. **17**, 627 (2021).

[11] Y.-R. Shen, *Principles of Nonlinear Optics* (Wiley-Interscience, New York, 1984).

[12] P. Hamm and M. Zanni, *Concepts and Methods of 2D Infrared Spectroscopy* (Cambridge University Press, Cambridge, UK, 2011).

[13] S. Mukamel, *Principles of Nonlinear Optical Spectroscopy*, Vol. 6 (Oxford University Press, Oxford, 1999).

[14] J. Lu, Y. Zhang, H. Y. Hwang, B. K. Ofori-Okai, S. Fleischer, and K. A. Nelson, Proc. Natl. Acad. Sci. U.S.A. **113**, 11800 (2016).

[15] J. Lu, X. Li, H. Y. Hwang, B. K. Ofori-Okai, T. Kurihara, T. Suemoto, and K. A. Nelson, Phys. Rev. Lett. **118**, 207204 (2017).

[16] Y. Wan and N. P. Armitage, Phys. Rev. Lett. **122**, 257401 (2019).

[17] Z.-L. Li, M. Oshikawa, and Y. Wan, Phys. Rev. X **11**, 031035 (2021).

[18] W. Choi, K. H. Lee, and Y. B. Kim, Phys. Rev. Lett. **124**, 117205 (2020).

[19] R. M. Nandkishore, W. Choi, and Y. B. Kim, Phys. Rev. Res. **3**, 013254 (2021).

[20] M. Fava, S. Biswas, S. Gopalakrishnan, R. Vasseur, and S. Parameswaran, Proc. Natl. Acad. Sci. U.S.A. **118**, e2106945118(2021).

[21] S. Woutersen, R. Pfister, P. Hamm, Y. Mu, D. S. Kosov, and G. Stock, J. Chem. Phys. **117**, 6833 (2002).

[22] M. Cho, Chem. Rev. **108**, 1331 (2008).

[23] Z. Terranova and S. Corcelli, J. Phys. Chem. B **118**, 8264 (2014).

[24] S. Paeckel, T. Köhler, A. Swoboda, S. R. Manmana, U. Schollwöck, and C. Hubig, Ann. Phys. (NY) **411**, 167998 (2019).

[25] L. Vanderstraeten, F. Verstraete, and J. Haegeman, Phys. Rev. B **92**, 125136 (2015).

[26] A. K. Bera, B. Lake, F. H. L. Essler, L. Vanderstraeten, C. Hubig, U. Schollwöck, A. T. M. N. Islam, A. Schneidewind, and D. L. Quintero-Castro, Phys. Rev. B **96**, 054423 (2017).

[27] L. Vanderstraeten, M. Van Damme, H. P. Büchler, and F. Verstraete, Phys. Rev. Lett. **121**, 090603 (2018).

[28] M. Van Damme, R. Vanhove, J. Haegeman, F. Verstraete, and L. Vanderstraeten, Phys. Rev. B **104**, 115142 (2021).

[29] M. Fava, R. Coldea, and S. Parameswaran, Proc. Natl. Acad. Sci. U.S.A. **117**, 25219 (2020).

[30] C. Morris, N. Desai, J. Viirok, D. Hüvonen, U. Nagel, T. Room, J. Krizan, R. Cava, T. McQueen, S. Koohpayeh *et al.*, Nat. Phys. **17**, 832 (2021).

[31] S. Lee, R. K. Kaul, and L. Balents, Nat. Phys. **6**, 702 (2010).

[32] A. W. Kinross, M. Fu, T. J. Munsie, H. A. Dabkowska, G. M. Luke, S. Sachdev, and T. Imai, Phys. Rev. X **4**, 031008 (2014).

[33] Y. Xu, L. S. Wang, Y. Y. Huang, J. M. Ni, C. C. Zhao, Y. F. Dai, B. Y. Pan, X. C. Hong, P. Chauhan, S. M. Koohpayeh, N. P. Armitage, and S. Y. Li, Phys. Rev. X **12**, 021020 (2022).

[34] J. A. Kjäll, F. Pollmann, and J. E. Moore, Phys. Rev. B **83**, 020407(R) (2011).

[35] B. M. McCoy and T. T. Wu, Phys. Rev. D **18**, 1259 (1978).

[36] R. Coldea, D. Tennant, E. Wheeler, E. Wawrzynska, D. Prabhakaran, M. Telling, K. Habicht, P. Smeibidl, and K. Kiefer, Science **327**, 177 (2010).

[37] C. M. Morris, R. Valdés Aguilar, A. Ghosh, S. M. Koohpayeh, J. Krizan, R. J. Cava, O. Tchernyshyov, T. M. McQueen, and N. P. Armitage, Phys. Rev. Lett. **112**, 137403 (2014).

[38] S. Rutkevich, J. Stat. Mech.: Theory Exp. (2010) P07015.

[39] S. Rutkevich, J. Stat. Phys. **131**, 917 (2008).

[40] S. Shinkevich and O. F. Syljuåsen, Phys. Rev. B **85**, 104408 (2012).

[41] M. Kormos, M. Collura, G. Takács, and P. Calabrese, Nat. Phys. **13**, 246 (2017).

[42] F. Liu, R. Lundgren, P. Titum, G. Pagano, J. Zhang, C. Monroe, and A. V. Gorshkov, Phys. Rev. Lett. **122**, 150601 (2019).

[43] G. Vidal, Phys. Rev. Lett. **91**, 147902 (2003).

[44] G. Vidal, Phys. Rev. Lett. **93**, 040502 (2004).

[45] G. Vidal, Phys. Rev. Lett. **98**, 070201 (2007).

[46] S. M. Kogan, Sov. Phys. JETP **16**, 217 (1963).

[47] W. J. Caspers, Phys. Rev. **133**, A1249 (1964).

[48] F. Bassani and S. Scandolo, Phys. Rev. B **44**, 8446 (1991).

[49] R. Verdel, F. Liu, S. Whitsitt, A. V. Gorshkov, and M. Heyl, Phys. Rev. B **102**, 014308 (2020).

[50] H. Zou, Y. Cui, X. Wang, Z. Zhang, J. Yang, G. Xu, A. Okutani, M. Hagiwara, M. Matsuda, G. Wang *et al.*, Phys. Rev. Lett. **127**, 077201 (2021).

[51] Q. Faure, S. Takayoshi, S. Petit, V. Simonet, S. Raymond, L.-P. Regnault, M. Boehm, J. S. White, M. Månsson, C. Rüegg *et al.*, Nat. Phys. **14**, 716 (2018).

[52] M. Fava, S. Gopalakrishnan, R. Vasseur, F. H. L. Essler, and S. A. Parameswaran, arXiv:2208.09490.

[53] O. Hart and R. Nandkishore, arXiv:2208.12817.

[54] J. Hauschild and F. Pollmann, SciPost Physics Lecture Notes, 5 (2018).

[55] I. P. McCulloch, arXiv:0804.2509.

[56] U. Schollwöck, Ann. Phys. (NY) **326**, 96 (2011).

[57] H. N. Phien, G. Vidal, and I. P. McCulloch, Phys. Rev. B **86**, 245107 (2012).

[58] A. Milsted, J. Haegeman, T. J. Osborne, and F. Verstraete, Phys. Rev. B **88**, 155116 (2013).

[59] M. Binder and T. Barthel, Phys. Rev. B **98**, 235114 (2018).

[60] S. Ejima, F. Lange, and H. Fehske, SciPost Phys. **10**, 077 (2021).